Dalton Transactions

ARTICLE

Dysprosium-based complexes with a flat pentadentate donor: a magnetic and *ab initio* study

Received 00th January 20xx,
Accepted 00th January 20xx

DOI: 10.1039/x0xx00000x

www.rsc.org/

Matilde Fondo,[a,*] Julio Corredoira-Vázquez,[a] Ana M. García-Deibe,[a] Silvia Gómez-Coca,[b] Eliseo Ruiz,[b] and Jesús Sanmartín-Matalobos[a]

The reactivity of the well-known pentadentate N_3O_2 Schiff base H_2L (2,6-bis(2-hydroxyphenyliminomethyl)pyridine) towards a lanthanoid metal, in this case Dy^{III}, has been investigated for the first time. This reactivity markedly depends on the pH of the medium and, accordingly, two different complexes, $[Dy(HL)(NO_3)_2]\cdot H_2O$ (**1**·H_2O) and $[Dy(L)(NO_3)(EtOH)(H_2O)]\cdot 2H_2O$ (**2**·$2H_2O$), could be isolated from dysprosium(III) nitrate and H_2L. In addition, reaction of H_2L with dysprosium(III) chloride in methanol yields $[Dy(HL')_2)][Dy(L)(Cl_2)]$ (**3**), where H_2L' (6-(2-hydroxyphenyliminomethyl)-2-methoxyhydroxymethyl)pyridine) is an N_2O_2 hemiacetal donor derived from the partial hydrolysis of the H_2L ligand, and subsequent addition of the methanol solvent to the carbonyl group. This latter reaction has been firstly observed for a lanthanoid metal. Single crystal X-ray diffraction studies of **1**·$1.15Py\cdot 0.3CH_3C_6H_5$, **2**·$2H_2O$ and **3** show that the Schiff base is acting as a nearly flat pentadentate donor in all the cases, being this behaviour independent of the deprotonation degree of the phenolic oxygen atoms, both mono- or bisdeprotonated. Complexes **1**·$1.15Py\cdot 0.3CH_3C_6H_5$ and **2**·$2H_2O$ show DyN_3O_6 cores, with distorted geometries closer to spherical tricapped trigonal prism or spherical capped square antiprism for **1**·$1.15Py\cdot 0.3CH_3C_6H_5$ and **2**·$2H_2O$, respectively. In the case of **3**, the $[Dy(HL')_2)]^+$ cation shows a dysprosium ion in an N_4O_4 triangular dodecahedron environment, while the $[Dy(L)(Cl_2)]^-$ anion displays a $DyN_3O_2Cl_2$ core with distorted pentagonal bipyramidal geometry. Moreover, attempts to dilute **1**·H_2O with yttrium yielded single crystals of $(Et_3NH)[Dy_{0.09}Y_{0.91}(L)(NO_3)_2]$ (**4**), where the Schiff base shows a similar pentadentate coordination mode. Dynamic magnetic studies of **1**·H_2O, **2**·$2H_2O$ and **3** show that **2**·$2H_2O$ and **3** present field-induced slow relaxation of the magnetisation, with U_{eff} barriers of 46.1(9) and 31.0(7) K for **2**·$2H_2O$ and **3**, respectively, while **1**·H_2O does not exhibit frequency-dependent peaks of the out of phase susceptibility, even in the presence of an external dc magnetic field. By contrast, the dilute sample **4** behaves as a SIM at zero dc field, with an energy barrier of *ca.* 49 K. *Ab initio* calculations using CASSCF methods including spin-orbit effects qualitatively support the obtained magnetic results, indicating that axiality is not the only factor that should be taken into account in order to increase effective energy barrriers.

Introduction

The coordination chemistry of trivalent lanthanoid ions has attracted a profound interest in recent years because of the unique combination of optical and magnetic properties displayed by 4f metals.[1] Regarding to magnetism, their potential high magnetic moments, along with the magnetic anisotropy due to the unquenched orbital angular momentum of unpaired 4*f* electrons, make them unique for the development of magnetic materials.[2] In fact, Ln^{III} ions have been widely used as key elements for producing hard permanent magnets, such as FeNdB. However, the discovery of the first Single Ion Magnet (SIM), the bis-phtalocyanine terbium complex $[Tb(Pc)_2]$, reported by Isikawa and *col.* in 2003[3] has triggered an outbreak in the synthesis of lanthanoid complexes and the study of their magnetic properties.

Nowadays, the search of high performance molecule magnets goes on being a very active research field. Many are the achievements of this area over the last 10 years, and among them, the publication of the electrostatic model for increasing the anisotropy in single ion *f*-metal complexes by Reinhart and Long[4] has meant taking a step forward. According to this theory, as well as some considerations on the ground state, and the Kramer or non-Kramer nature of the metal ion, it is supposed that the best magnetic results should be achieved by mononuclear dysprosium(III) compounds with an axial geometry. As a result, the area of SIMs has been increasingly focused on isolating Dy^{III} compounds with such axial geometry.[5,6]

An intensive research, with a huge amount of lanthanoid complexes synthesised, has harvested outstanding results leading to a significant improvement in the magnetic properties of SIMs, with a constant increase both in the blocking temperatures (T_B) and in the effective energy barriers (U_{eff}). Thus, in 2016, 20 K was the T_B

---

[a] Departamento de Química Inorgánica, Facultade de Química, Universidade de Santiago de Compostela, 15782 Santiago de Compostela, Spain
E-mail: matilde.fondo@usc.es.
[b] Departament de Química Inorgànica i Orgànica, and Institut de Química Teórica i Computacional, Universitat de Barcelona, 08028 Barcelona, Spain

Electronic Supplementary Information (ESI) available: Tables S1-S8 and Figures S1-S19. CCDC 1942683 (**1**·$Py\cdot 0.5CH_3OH\cdot 0.5H_2O$), 1942684 (**2**·$2H_2O$), 1957820 (**3**) and 1942685 (**4**). For ESI and crystallographic data in CIF format see DOI: 10.1039/x0xx00000x.

record for the air stable pentagonal bipyramidal complex $[Dy(Cy_3PO)_2(H_2O)_5]Br_3$, reported by Tong and *col.,*[7] but this record was broken by the $[(Cp^{iPr5})Dy(Cp^*)][B(C_6F_5)_4]$ (Cp^{iPr5} = pentaisopropylcyclopentadienyl) metallocene, reported by Layfield *et al* in 2018,[8] with an amazing $T_B = 80$ K. This latter complex also holds the U_{eff} record of 1541 cm^{-1} (2217 K). This blocking temperature over the liquid nitrogen temperature, which has not yet been surpassed, means a milestone in the field of molecular magnetism.

In light of these findings, the search of SMMs of high blocking temperature should be focused on the organometallic chemistry of dysprosium. Nevertheless, a handicap of the related metallocenes seems to be their air sensitivity, as they need to be synthesised under strict inert conditions.[8-11]

Accordingly, the coordination chemistry of dysprosium(III) could provide a sound alternative, since coordination compounds are usually more stable in air, and some of them with SMM behaviour also display high blocking temperatures and/or energy barriers.[7,12]

With these considerations in mind, in order to deepen in some aspects of the coordination chemistry of lanthanoids, as well as in its magnetism, we decided to investigate the coordination ability of a well-known flat pentadentate and highly stable ligand, H_2L (Scheme 1)[13] with dysprosium(III) ions. It should be noted that the coordination chemistry of this Schiff base with *d*-block[14-21] metals and tin[13] has been rather studied but, to the best of our knowledge, its interaction with lanthanoid metals is hitherto unknown. Thus, in this work we report the reactivity of H_2L towards dysprosium, analysing the influence of the operational pH, as well as the salt employed. The dynamic magnetic behaviour of the obtained complexes is also reported, while the magnetic results are explained in the light of *ab initio* calculations.

Experimental

Materials and general methods

All chemical reagents were purchased from commercial sources, and used as received without further purification. Elemental analyses of C, H and N were performed on a Carlo Erba EA 1108 analyser. Infrared spectra were recorded in the ATR mode on a Varian 670 FT/IR spectrophotometer in the range 4000-500 cm^{-1}. The ^{1}H NMR spectrum of H_2L was recorded on a Bruker DPX-250 spectrometer. Micro X-ray fluorescence quantitative analyses of Y and Dy for **4** were recorded on a Bruker TORNADO 4 device.

Syntheses of the H_2L

H_2L was obtained as a highly pure yellow solid by a variation of a previously described method,[13] where the ethanol solvent of the reaction was changed by a mixture of chloroform and ethanol. The ligand was satisfactorily characterised by elemental analysis, IR and ^{1}H NMR spectroscopy. Yield: 97%. M.W.: 317. Anal. calcd. for $C_{19}H_{15}O_2N_3$: C 71.92, N 13.25, H 4.73 %. Found: C 71.70, N 13.21, H 4.95 %. IR (ATR, $\tilde{\nu}$/cm^{-1}): 1585 (C=N$_{py}$), 1624 (C=N$_{imine}$), 3352, 3400 (OH). ^{1}H-RMN (DMSO-d_6, 250 MHz, δ in ppm): 6.94-6.96 (m, 4H), 7.15 (t, 2H), 7.35 (d, 2H), 8.11 (t, 1H), 8.51 (d, 2H), 8.81 (s, 2H), 9.13 (s, 2H).

Syntheses of the complexes

$[Dy(HL)(NO_3)_2]\cdot H_2O$ (**1**$\cdot H_2O$): A solution of $Dy(NO_3)_3\cdot 6H_2O$ (0.161 g, 0.353 mmol) in ethanol 96% (10 mL) was added to a yellow solution of H_2L (0.112 g, 0.353 mmol) in ethanol 96% (22 mL). The red mixture was refluxed for 3 h, and the resulting suspension was centrifuged. The mother liquor was decanted and the red solid dried in an oven. Yield: 0.111 (51%). Elemental analysis calcd. for $C_{19}H_{16}DyN_5O_9$ (620.50): C 36.74, N 11.28, H 2.58 %. Found: C 36.81, N 11.06, H 2.49 %. IR (ATR, $\tilde{\nu}$/cm^{-1}): 1269, 1475 (NO_3), 1543 (C=N$_{py}$), 1587 (C=N$_{imine}$), 3552 (OH).

The same solid was obtained when an ethanol solution of the ligand was basified with tetramethylammonium hydroxide up to an operational pH = 9.4, and then mixed with the dysprosium nitrate in similar conditions.

Recrystallisation of the red solid in pyridine/methanol/toluene by diffusion of diethylether yielded single crystals of $[Dy(HL)(NO_3)_2]\cdot 1.15Py\cdot 0.3CH_3C_6H_5$ (**1**$\cdot 1.15Py\cdot 0.3CH_3C_6H_5$), suitable for X-ray diffraction studies.

$[Dy(L)(NO_3)(EtOH)(H_2O)]\cdot 2H_2O$ (**2**$\cdot 2H_2O$): To a yellow solution of H_2L (0.094 g, 0.296 mmol) in ethanol 96% (30 mL), $(CH_3CH_2)_3N$ (6 mL, 0.600 mmol) was added, and an orange solution was obtained. Then, a solution of $Dy(NO_3)_3\cdot 6H_2O$ (0.14 g, 0.307 mmol) in ethanol 96% (10 mL) was incorporated, and the red mixture was refluxed with stirring for 3 h. The resultant red solution was filtered to avoid possible impurities, and the filtrate was concentrated up to 20 mL. The obtained suspension was centrifuged, the mother liquors decanted, and the red solid dried in an oven. Yield: 0.049 g (25%). Elemental anal. calcd. for $C_{21}H_{25}DyN_4O_9$ (639.95): C 39.38, N 8.75, H 3.91 %. Found: 39.18, N 8.85, H 4.04 %. IR (ATR, $\tilde{\nu}$/cm^{-1}): 1269, 1455 (NO_3), 1534 (C=N$_{py}$), 1585 (C=N$_{imine}$), 3230, 3483, 3541 (OH).

Slow evaporation of the mother liquor yielded single crystals suitable for X-ray diffraction studies of **2**$\cdot 2H_2O$.

$[[Dy(HL')_2)][Dy(L)(Cl_2)]$ (**3**): To a solution of H_2L (0.112 g, 0.353 mmol) in methanol (23 mL) with operational pH = 6.5, a methanol solution of Me_4NOH 0.5 M was added up to operational pH = 7.2, changing the colour of the solution from yellow to light orange. Then, $DyCl_3\cdot 6H_2O$ (0.133 g, 0.353 mmol) was incorporated and the red mixture was stirred while refluxing with for 3 h. During this time, a red solid was formed, which was collected by filtration, and dried in air. Yield: 0.065 g (30%). Elemental analysis calcd. for $C_{47}H_{39}Dy_2Cl_2N_7O_8$ (1225.75): C 46.01, N 7.99, H 3.18 %. Found: 45.97, N 7.89, H 3.04 %. IR (ATR, $\tilde{\nu}$/cm^{-1}): 1539 (C=N$_{py}$), 1583 (C=N$_{imine}$), 3327 (OH).

Recrystallisation of the crude product in methanol/hexane yielded single crystals of **3**, suitable for X-ray diffraction studies

$(Et_3NH)[Dy_{0.09}Y_{0.91}(L)(NO_3)_2]$ (**4**): To a solution of H_2L (0.07 g, 0.221 mmol) in ethanol 96% (25 mL), $(CH_3CH_2)_3N$ (4.4 mL, 0.442 mmol) was added. Subsequently, a solution of $Dy(NO_3)_3\cdot 6H_2O$ (0.01 g, 0.0219 mmol) and $Y(NO_3)_3\cdot 6H_2O$ (0.076 g, 0.198 mmol) in ethanol 96% (10 mL) was incorporated to the basic light orange ligand solution, and the mixture was refluxed with stirring for 3 h. The resultant intense orange solution was filtered to avoid possible impurities, and the filtrate was slowly evaporated until the appearance of orange single crystals of $(Et_3NH)[Dy_{0.09}Y_{0.91}(L)(NO_3)_2]$, and which resulted suitable for X-ray diffraction studies, precipitated. The crystals were separated from the solution by filtration, and dried in air. Yield: 0.07 g (50%). Elemental analysis calcd. for $C_{25}H_{29}Dy_{0.09}N_6O_8Y_{0.91}$ (637.44): C 47.06, N 13.18, H 4.55 %. Found: C 47.21, N 13.06, H 4.79 %. Micro X-ray fluorescence: Dy:Y ratio 0.09: 0.91.

Crystallographic refinement and structure solution

Crystal data and some details of the refinement are given in Table S1. Single crystals of **1**·1.15Py·0.3$CH_3C_6H_5$, **2**·2H_2O, **3** and **4** were obtained as detailed above. Data were collected at 100 K on a Bruker D8 VENTURE PHOTON III-14 diffractometer, employing graphite monochromatised Mo-kα (λ = 0.71073 Å) radiation. Multi-scan absorption corrections were applied using SADABS.[22] Diffraction data of **3** showed twinning, and they were treated as a four-component twin with scales: 0.396(6), 0.302(3), 0.186(4) and 0.116(4). These structures were solved by standard direct methods, employing SHELXT,[22] and then refined by full matrix least-squares techniques on F^2, using SHELXL from the program package SHELX-2018.[23]

All non-hydrogen atoms corresponding to the complexes were refined anisotropically, but in some cases disordered atoms or solvates with low occupation sites were isotropically treated. Hydrogen atoms were typically included in the structure factor calculations in geometrically idealised positions. Hydrogen atoms attached to oxygen and/or nitrogen atoms, were located in the corresponding Fourier maps, with the intention of revealing the hydrogen bonding scheme. In this case, either they were freely refined, or with thermal parameters derived from their parent atoms.

In the case of **1**·1.15Py·0.3$CH_3C_6H_5$, the treatment of the H atom involved in the strong interaction existing between one of the phenol O atoms of the ligand (O2) and the solvated pyridine molecule, with an intermolecular O2···N1s distance of only 2.513(3) Å, deserved a particular attention. The position of this H atom was very significant, as it meant the difference between an O−H···N or an N−H···O interaction. This difference would also imply a different nature of both the complex (neutral or anionic) and the solvated molecule (pyridine or pyridinium cation). Although residual charges could be found in the Fourier map at plausible positions near to O2 and N1s, a first disorder model with calculated 67 and 34% occupation sites was attempted, but an isotropic refinement of these two disordered H atoms resulted not adequate. This fact, in joint with the clear asymmetry of the Dy-O and O-C_{phen} bonds in the complex, which is indicative of a phenol more than a phenolate behaviour for O2, and their accordance with others found in the literature for Dy^{III} complexes with phenol ligands (Table S2), led to choose a refinement with a fully occupied phenol H atom, with the aim of simplifying the resulting formula to $[Dy(HL)(NO_3)_2]$·1.15Py·0.3$CH_3C_6H_5$, and keeping more similarity with the nature of the crude solid **1**·H_2O, which was used for magnetic measurements.

Some disorder could be appreciated in some phenyl rings of one of the molecules present in **3**, in particular in **3a**, but being a 4-component twinned crystal, the quality of data avoided to model this disorder adequately.

The crystallographic data of **4** correspond to a crystal that contains analogue complexes of Dy and Y ions in a ratio of 0.09:0.91, which are randomly distributed in the crystal. This proportion was determined according to their calculated occupation sites in each molecule of the complex. This proportion was also corroborated by Micro X-ray fluorescence techniques.

Powder X-ray diffraction studies

The powder diffractograms of **2**·2H_2O, **3** and **4** were recorded in a Philips diffractometer with a control unity type "PW1710", a vertical goniometer type "PW1820/00" and a generator type "Enraf Nonius FR590", operating at 40 kV and 30 mA, using monochromatised Cu-Kα (λ = 1.5418 Å) radiation. A scan was performed in the range $2 < 2\vartheta < 30°$ with t = 3 s and $\Delta 2\vartheta = 0.02°$. LeBail refinement was obtained with the aid of HighScore Plus Version 3.0d.

Magnetic measurements

Magnetic susceptibility dc and ac measurements for powder crystalline samples of **1**·H_2O, **2**·2H_2O, **3** and **4** were carried out at the Unitat de Mesures Magnètiques of the Universitat de Barcelona with a Quantum Design SQUID MPMS-XL susceptometer. The dc magnetic susceptibility data were recorded under magnetic fields of 190 G (2-30 K) and 3000 G (30-300 K) in the range 2-300 K. Magnetisation measurements at 2.0 K were recorded under magnetic fields ranging from 0 to 50000 Oe. Diamagnetic corrections were estimated from Pascal's Tables. Alternating current (ac) susceptibility measurements under different applied static fields (H_{dc} = 0, 1500 or 3000 Oe) were performed with an oscillating ac field of 3.5 Oe and ac frequencies ranging from 4 to 1500 Hz.

Computational Details

CASSCF method was employed to calculate the state energies without spin-orbit effects for mononuclear Dy(III) complexes, while the effect of spin–orbit coupling was taken into account perturbatively in a second step by using the restricted active space state interaction method (RASSI).[24] Dynamic correlation contributions are not essential due to the relatively large ionic character of the Ln-O bonds. The MOLCAS ANO-RCC basis set[25-27] was used for all the atoms. The following contractions were used: Dy [9s8p6d4f3g2h]; Cl [5s4p3d2f]; O [4s3p2d1f]; N [4s3p2d1f]; C [3s2p] and H [2s]. In the CASSCF calculations, a (9,7) active space were used by considering 21 sextets, 128 quadruplets and 98 doublets. The direction and magnitude of the magnetic moment of the final states were evaluated using the SINGLE_ANISO routine implemented in open Molcas.[28] The matrix elements of the transition magnetic moments have been calculated to have an estimation about the probability of transition between two different states of the molecules.[29] Such matrix elements are calculated as proposed by the golden Fermi rule, as the integral between the two involved states using a magnetic moment operator.

Results and discussion

The reactivity of H_2L towards $Dy(NO_3)_2·6H_2O$ was investigated under different reaction conditions, as shown in Scheme 1. Thus, when H_2L and $Dy(NO_3)_3·6H_2O$ were mixed in 1:1 molar ratio in ethanol 96%, the quite insoluble complex **1**·H_2O precipitates. The same compound was also obtained when an ethanol solution of the ligand, basified with tetramethylammoniun hydroxide up to operational pH = 9.4, was mixed with the dysprosium salt in 1:1 molar ratio. Nevertheless, if an ethanol solution of H_2L was mixed with Et_3N in 1:2 molar ratio, and then $Dy(NO_3)_2 \cdot 6H_2O$ was added (1:1 ligand:salt molar ratio), the very soluble complex **2**·$2H_2O$ was isolated.

Reaction of $DyCl_3 \cdot 6H_2O$ with a solution of H_2L, basified with tetramethylammoniun hydroxide up to operational pH = 7.2, leads to the ionic complex $[Dy(HL')_2)][Dy(L)(Cl_2)]$ (**3**) (Scheme 1). This ionic compound, composed of $[Dy(HL')_2)]^+$ cations and $[Dy(L)(Cl_2)]^-$ anions, where the dysprosium ion in the cation is surrounded by two $(HL')^-$ ligands. These latter ligands, showing a hemiacetal functional group, derived from the Schiff base L^{2-} (Scheme S1). The formation of hemiacetals from aldehydes and alcohols is quite well known, as these are usually developed as intermediates in the preparation of acetals from aldehydes or ketones. However, hemiacetals are rather unstable species, and only very small amounts can be obtained if they are not stabilised by structural effects.[30]

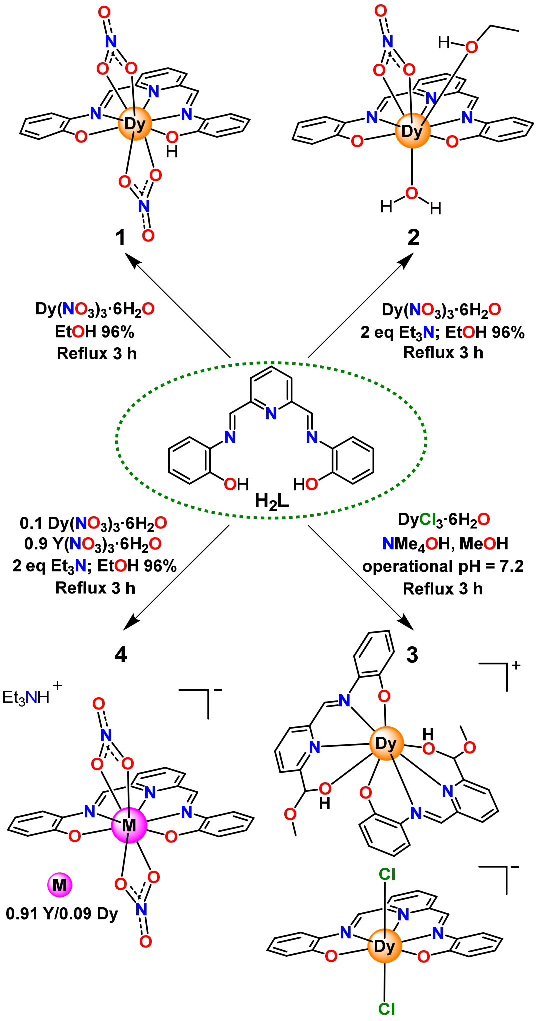

Scheme 1. Reaction scheme for obtaining complexes **1**-**4**.

Only a few crystal structures of complexes containing hemiacetals as ligands have hitherto been reported. These scarce examples usually contain d-metals[31-36] but, to the best of our knowledge, no hemiacetal complexes have been described with lanthanoid metal ions. Besides, most of the reported complexes were obtained by conversion of aldehydes, and, so far as we know, only one case was reported where the hemiacetal donor comes from an imine ligand.[34] The process concerning the conversion of imines into hemiacetals (Scheme S1), seems to be catalysed by coordination to the metal ion.[34] This can be readily inferred from the fact that the Schiff base H_2L is obtained in alcohols without any evidence of decomposition in this or related works.[13] Nevertheless, the operational pH of the medium and/or the presence of chloride in the reaction medium must play an important role in the formation of the hemiacetal from solvolysis of the coordinated imine, given that the Schiff base is intact in complexes **1**·H_2O and **2**·$2H_2O$. The efforts made to carry out the same reaction in a non-alcoholic medium, such as acetonitrile or THF, were unfruitful, and the isolated solids could not be satisfactorily characterised.

Moreover, with the aim of obtaining a diluted sample of **1**·H_2O, several were the synthetic routes attempted. Thus, mixtures of H_2L and $Dy(NO_3)_2 \cdot 6H_2O$ and $Y(NO_3)_2 \cdot 6H_2O$ in similar reaction conditions to those used in the two methods that allowed isolating **1**·H_2O, yielded red solids that could not be adequately characterised. Additional multiple attempts made varying the operational pH of the medium, with either Me_4NOH or Et_3N, have not led to the desired neutral $[Dy_{0.09}Y_{0.91}(HL)(NO_3)_2]$. By contrast, when these reactions were repeated with addition of two equivalents of Et_3N to the H_2L solution, orange single crystals of $Et_3NH[Dy_{0.09}Y_{0.91}(L)(NO_3)_2]$ (**4**) could be easily isolated.

In addition, efforts were also made to obtain an yttrium analogue of **1**·H_2O by using similar reaction conditions, just changing the dysprosium nitrate by yttrium nitrate. Nevertheless, these syntheses do not produce the desired $[Y(HL)(NO_3)_2]$ complex either, as the obtained solids could not be satisfactorily characterised. Likewise, mixing H_2L, Et_3N and yttrium nitrate in molar ratios 1:2:1, in a completely analogous procedure to that used to isolate **2**·$2H_2O$, did not allow obtaining the yttrium analogue of **2** $[Y(L)(NO_3)(EtOH)(H_2O)]$ either.

The **1**·H_2O - **4** complexes were unequivocally characterised by analytical techniques and IR spectroscopy, and their magnetic behaviour was also analysed. Furthermore, crystals of **1**·$1.15Py \cdot 0.3CH_3C_6H_5$, **2**·$2H_2O$, **3** and **4**, obtained as described above, were studied by single crystal X-ray diffraction studies.

The infrared spectra of **1**·H_2O, **2**·$2H_2O$ and **3** show two intense bands at *ca*. 1585 and 1540 cm^{-1}, assigned to ν(C=N) vibrations of the imine and pyridine moieties, respectively,[37] which undergo negative shifts respect to the free ligand, indicating that both the imine and pyridine nitrogen atoms are coordinated to the metal ion. The spectra of **1**·H_2O and **2**·$2H_2O$ also show two strong bands at *ca*. 1270 and 1460 cm^{-1}, in agreement with the presence of bidentate nitrate ligands.[37] In addition, broad bands in the range 3200-3600 cm^{-1} agree with the existence of coordinated or solvated water and/or ethanol. In the case of **3**, the spectrum shows one quite sharp band at 3327 cm^{-1}, assigned to the non-deprotonated alcohol function of the hemiacetal group.

X-ray diffraction studies

An ellipsoid diagram for **1** is shown in Fig. 1, and main distances and angles are given in Table S3. The unit cell of **1**·$1.15Py \cdot 0.3CH_3C_6H_5$ contains neutral $[Dy(HL)(NO_3)_2]$ molecules, in addition to solvated pyridine and toluene.

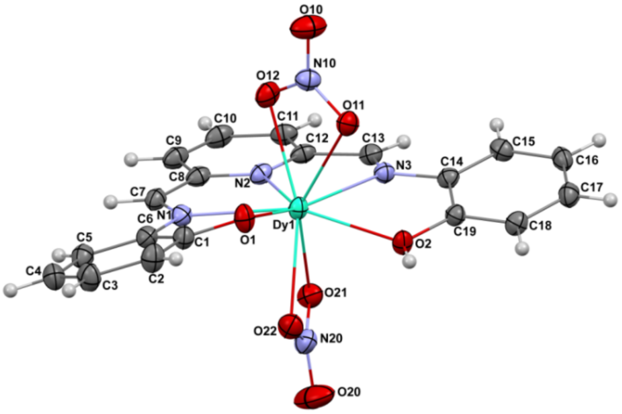

Fig. 1. Ellipsoid (50% probability) diagram for **1**.

In $[Dy(HL)(NO_3)_2]$, the monoanionic HL$^-$ Schiff base acts as a pentadentate N_3O_2 donor. In spite of the conjugation and, therefore, nearly planar character of the ligand, it adopts a helical disposition in this complex. Hence, the oxygen atoms O1 and O2 are the most prominent ones from the mean N_3O_2 calculated plane, and they are *ca*. 0.39 Å above or below this plane.

The coordination sphere of the dysprosium atom is completed by two nitrate ligands, acting as bidentate chelate donors, which are rotated with respect to each other, in such a way that the NO_2 calculated planes form an angle of *ca*. 60.8 °. Consequently, the dysprosium centre has coordination number 9. Calculations of the degree of distortion of the DyN_3O_6 core with respect to an ideal nine vertex polyhedron with the SHAPE software,[38] gives rise to shape measurements closer to spherical tricapped trigonal prism (Fig. S1, Table S4).

All the bond distances and angles around the dysprosium(III) ion are in their normal ranges.[39] However, it is noteworthy that the Dy1-O2 distance is significantly longer than that observed for Dy1-O1, what is in agreement with the monodeprotonation of the Schiff base, where O2 remains protonated.

The $[Dy(HL)(NO_3)_2]$ molecules in the cell are quite far away, and the shortest intermolecular Dy···Dy distance is 8.1298(7) Å.

The unit cell of $\mathbf{2}\cdot 2H_2O$ contains $[Dy(L)(NO_3)(H_2O)(EtOH)]$ molecules (Fig. 2), as well as some solvated water molecules.

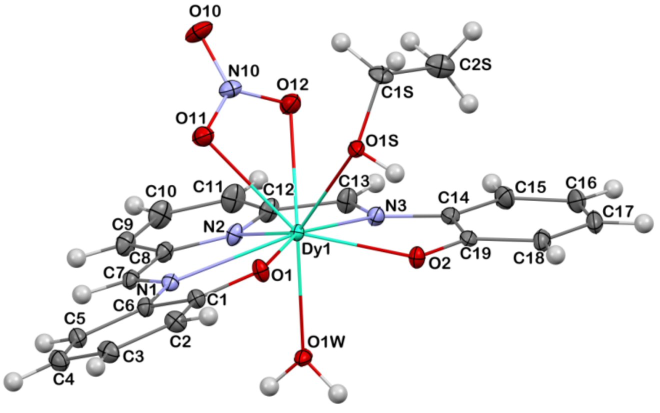

Fig. 2. Ellipsoid (50% probability) diagram for **2**.

The structure of $[Dy(L)(NO_3)(H_2O)(EtOH)]$ is quite similar to that of $[Dy(HL)(NO_3)_2]$, but with some significant differences. Thus, in the same way as in **1**, the Schiff base, which now is dianionic, acts as a pentadentate N_3O_2 donor. Nevertheless, the multidentate ligand has now an umbrella like distortion, with the dysprosium atom *ca*. 0.42 Å above the mean calculated N_3O_2 plane. The coordination sphere around Dy^{III} is completed by a bidentate chelate nitrate donor, one water and one ethanol molecule, leading to coordination number 9. In this case, calculations of the distortion from an ideal DyN_3O_9 core with the SHAPE program[38] indicate that the geometry is closer to a spherical capped square antiprism, but highly distorted towards muffin (Fig. S1, Table S4). The main distances and angles about the metal centre agree with those expected for this kind of compound.[39] Since Dy1-O1 and Dy1-O2 are quite similar in this case, and shorter than Dy1-O2 in complex **1** (Table S3), this behaviour is in agreement with a full deprotonation of both phenol oxygen atoms in **2**.

Finally, it should be noted that the phenolic oxygen atoms, the nitrate ligand, coordinated water and ethanol, and water solvates are implicated in a complex hydrogen bond scheme, which expands the initial molecule into a 3D grid, where the shortest intermolecular Dy···Dy distance is 6.4395(5) Å.

An ellipsoid diagram for **3** is shown in Fig. 3 and main distances and angles are recorded in Table S5. The crystal structure of **3** shows that it is an ionic compound, composed of $[Dy(L')_2)]^+$ cations (**3a**) and $[Dy(L)(Cl_2)]^-$ anions (**3b**).

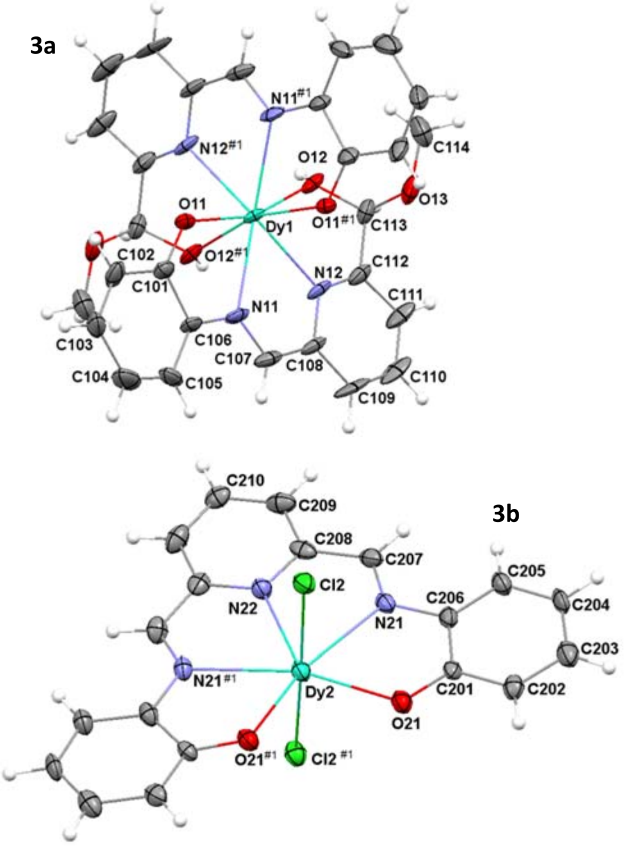

Fig. 3. Ellipsoid (30% probability) diagram for **3**: top) cation **3a**; bottom) anion **3b**.

In the **3a** cation (Fig. 3), the dysprosium ion is surrounded by two imine-hemiacetal ligands that act as monoanionic N_2O_2 donors, by means of the nitrogen atoms of the imine (N11) and pyridine (N12) functions, the deprotonated phenolic oxygen atom (O11), and the protonated alcoholic oxygen atom (O12) of the hemiacetal group. Accordingly, the Dy^{III} centre is octa-coordinate in an N_4O_4

environment, with a calculated geometry close to triangular dodecahedron, but distorted towards snub disphenoid (Table S4, Fig. S2).[38] This cation has two chiral centres, the carbon atoms of the hemiacetal groups, but both *S*,*S* and *R*,*R* isomers of the **3a** cation are present in the unit cell in 1:1 ratio, thus giving rise to a racemic mixture.

In the **3b** anion (Fig. 3), the bisdeprotonated Schiff base L^{2-} wraps the dysprosium(III) centre in its N_3O_2 pocket, as in **1** and **2**. The coordination sphere is completed by two chloride anions, and, accordingly, the dysprosium ion achieves coordination number 7, with slightly distorted pentagonal bipyramid geometry (Table S4, Fig. 3). In this case, the pentadentate donor is nearly planar (maximum deviation of any atom from the mean calculated N_3O_2 plane of 0.112 Å, with the Dy atom in the plane), and the Cl-Dy-Cl angle is *ca*. 177°. All the distances and angles in this anion are similar to those found in a previously reported chloro-dysprosium anionic complex of a hydrazone ligand with a pseudo-pentagonal bipyramidal geometry.[40]

Besides, this structure is further stabilised by two short hydrogen bonds between the phenolic oxygen atoms of the **3b** anion and the protonated alcoholic functions of the **3a** cation, what generates a pseudodinuclear complex, with a $Dy^{III}\cdots Dy^{III}$ distance of *ca*. 5.486 Å (Fig. S3).

In addition, the crystal structure of the diluted complex $Et_3NH[Dy_{0.09}Y_{0.91}(L)(NO_3)_2]$ (**4**) was solved. An ellipsoid diagram of the compound is shown in Fig. S4, and main distances and angles are summarised in Table S6. In this case the complex is also ionic, the $[Dy_{0.09}Y_{0.91}(L)(NO_3)_2]^-$ anion and Et_3NH^+ cation being joined through a hydrogen bond between the nitrogen atom of the cation and one of the phenolic oxygen atoms of the anion. No other hydrogen bonds are observable in the cell, and the shortest distance between dysprosium or yttrium atoms of two neighbouring $[Dy_{0.09}Y_{0.91}(L)(NO_3)_2]^-$ anions is *ca*. 8.36 Å.

The structure of the $[Dy_{0.09}Y_{0.91}(L)(NO_3)_2]^-$ complex is similar to that described for $[Dy(HL)(NO_3)_2]$, with the Schiff base adopting a helical disposition, although in this case this ligand is fully deprotonated, with both phenol oxygen atoms negatively charged. The calculated environment of the yttrium and dysprosium ions in **4** with the SHAPE program is close to spherical tricapped trigonal prism (Table S4). Therefore, as all the distances and angles are in the expected range, this structure does not deserve further discussion.

Moreover, powder X-ray diffraction studies for the crude products $\mathbf{2}\cdot 2H_2O$, **3** and **4** (Figs. S5-S7) demonstrate that the microcrystalline product and the single crystals are the same compound in all cases, and, in the case of **3**, that the experiment is reproducible, given that two different experiments yield the same X-ray diffraction powder diffactogram.

It could be worthy to comment that the Dy^{III} complexes **1**-**4** are the first lanthanoid compounds of H_2L and related ligands to be crystallographically characterised, as only some tin and *d*-metal complexes resulting from H_2L or its derivatives were previously reported (Table S7, Scheme S2). A search from CSD data[41] (Table S7) shows that this type of ligand can usually act as dianionic, which is its most common charge, or as a neutral Schiff base, but it has only been described once as a monoanionic donor to date. In its dianionic form, the most common coordination modes are as a pentadentate μ_2 or μ_4 bridge, or as an N_3O_2 non-bridging chelating donor (Scheme S3). This latter one is the coordination mode found in all the lanthanoid complexes described herein, and it should be noted that the degree of deprotonation of the ligand found in **1** (monodeprotonated) is unique for H_2L.

Magnetic Properties

Direct-current (dc) magnetic susceptibility measurements were recorded for $\mathbf{1}\cdot H_2O$, $\mathbf{2}\cdot 2H_2O$ and **3** as a function of the temperature. The plots of $\chi_M T$ *vs* T for $\mathbf{1}\cdot H_2O$, $\mathbf{2}\cdot 2H_2O$ and **3** are shown in Fig. 4, and Figs. S8 and S9, respectively.

At 300 K, the $\chi_M T$ values are 14.07 cm^3Kmol^{-1} for $\mathbf{1}\cdot H_2O$, 14.13 cm^3Kmol^{-1} for $\mathbf{2}\cdot 2H_2O$ and 29.3 cm^3Kmol^{-1} for **3**, values that are very close to those expected for one or two isolated Dy^{3+} ions (14.13 cm^3Kmol^{-1} per ion). In all cases, the experimental $\chi_M T$ values remain almost constant when the temperature decreases up to 70 K. Below this temperature, the drop in the curves is more pronounced, and the molar susceptibilities reach minimum values of 8.84, 7.83 and 18.01 cm^3kmol^{-1} at 2 K for $\mathbf{1}\cdot H_2O$, $\mathbf{2}\cdot 2H_2O$ and **3**, respectively. This drop can be mainly ascribed to depopulation of the M_J sublevels of the Dy^{III} ion at low temperatures.

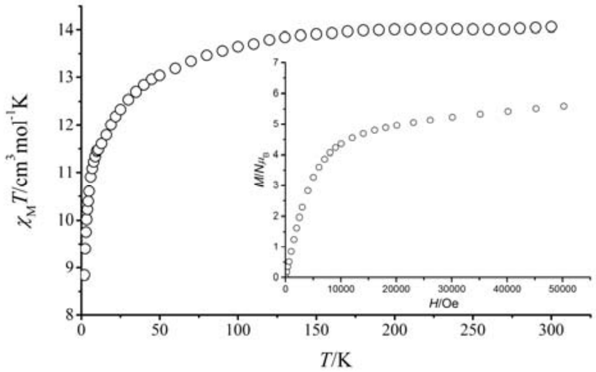

Fig. 4. $\chi_M T$ *vs* T for $\mathbf{1}\cdot H_2O$. Inset: $M/N\mu_B$ *vs* H.

Nevertheless, in the case of **3**, the drop below 13 K is even more marked and maybe the intermolecular interactions through the short hydrogen bonds between the anion and the cation play a role in this strong diminishment of the $\chi_M T$ value.

The reduced magnetisation at 2 K tends to 5.59 $N\mu_B$ for $\mathbf{1}\cdot H_2O$, 6.35 $N\mu_B$ for $\mathbf{2}\cdot 2H_2O$ and 10.45 $N\mu_B$ for **3** at maximum applied field of 5 T (Fig. 4, S8 and S9, inset). These values are considerable smaller than those expected for one or two isolated Dy^{III} centres (10 $N\mu_B$ per Dy^{3+} ion), but comparable with the values reported for many complexes per dysprosium centre,[39,42-45] what seems to agree with a significant magnetic anisotropy.

The low-temperature magnetic relaxation behaviour of complexes $\mathbf{1}\cdot H_2O$-**3** was studied. Thus, alternating current (ac) magnetic susceptibility measurements were initially recorded under a zero external field at a frequency of 1400 Hz. In this case, none of the compounds show out-of-phase ac susceptibilities (χ''_M) peaks. However, it is well known that these molecules can present quantum tunnelling (QTM) relaxation processes,[46] which prevent to observe the SMM behaviour. This QTM can be due to the intrinsic tunnelling between the states or induced by the dipolar intermolecular interactions. One way to partly or fully suppress this quantum tunnelling is the application of a small static magnetic field,[47] which should remove the degeneracy of the states, thus enabling observation of the slow relaxation process through the real thermally activated energy barrier.

Consequently, variable temperature ac susceptibilities were measured with the application of different dc fields. Under these conditions, **1**·H_2O shows ac susceptibility frequency and field dependence below 5 K, but without a maximum in its χ''_M curves (Fig. S10). Nevertheless, **2**·$2H_2O$ and **3** show χ''_M peaks as a function of the temperature at fixed frequencies, the optimal fields being 1500 Oe and 3000 Oe for **2**·$2H_2O$ and **3**, respectively (Fig. S11 and Fig. S12).

Complex **2**·$2H_2O$ shows frequency and temperature-dependence of the in phase (Fig. S13) and out-of-phase (Fig. 5) susceptibility under this field of 1500 Oe, with maxima for χ''_M between 4 and 6 K. Besides, it should be noted that χ''_M does not go to zero below the maxima at low temperature (Fig. 5), which indicates that the fast relaxation of the magnetisation by a QTM mechanism has not been fully suppressed by the application of the optimum magnetic field.

In addition, the Cole–Cole plot for **2**·$2H_2O$ (Fig. S14) displays semicircular shapes with α parameters in the range 0.18-0.08 (Table S8), which suggests more than one relaxation mechanism at low temperature.

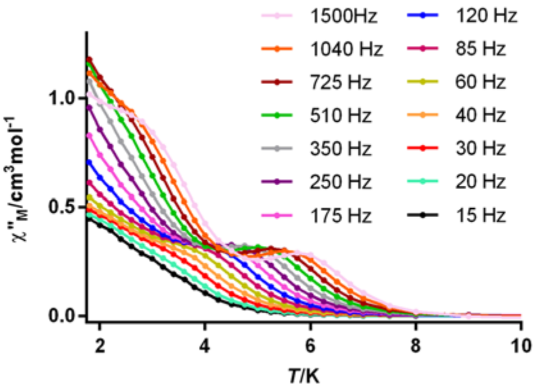

Fig. 5. Temperature dependence of χ_M'' for **2**·$2H_2O$ in a *dc* applied field of 1500 Oe at different frequencies.

The relaxation dynamics between 4 and 6 K were further analysed by studying the temperature dependence of the relaxation time. The deviation from linearity in the low-temperature region of the Arrhenius plot (Fig. 6) and the α parameter indicate that the curve cannot be reproduced with a simple Orbach model. Taking into account the experimentally observed QTM, attempts were made to fit this plot considering all the possible relaxation processes in addition to QTM (Orbach, Direct and Raman), but equation 1, which includes quantum tunnelling and Orbach thermal processes, is the one that best simulate this plot rendering reasonable parameters. This fit yields an effective energy barrier of 46.1(9) K, with a τ_0 factor of 5.0(2)x10^{-8} s and τ_{QTM} of 0.89 ms.

$$\tau^{-1} = \tau_{QTM}{}^{-1} + \tau_0{}^{-1} e^{-U_{eff}/k_B T} \quad (1)$$

χ'_M (Fig. S14) and χ''_M (Fig. 7) for **3** also show temperature and frequency dependence at the optimum external field of 3000 G (Figure S11).

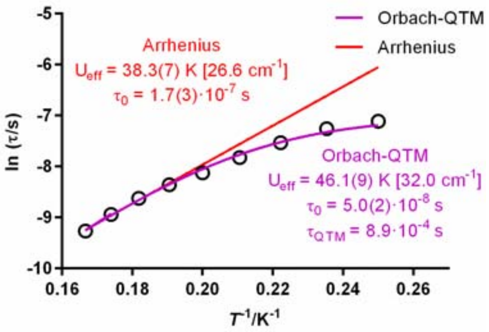

Fig. 6. Arrhenius plot for **2**·$2H_2O$ in a *dc* applied field of 1500 Oe. The violet line accounts for the best fit considering Orbach plus QTM relaxation (eq. 1).

The χ''_M plot versus *T* (Fig. 7) shows that χ''_M presents some peaks at different frequencies and, as in the case of **2**·$2H_2O$, it shows same tails at low temperature, also indicating the existence of QTM.

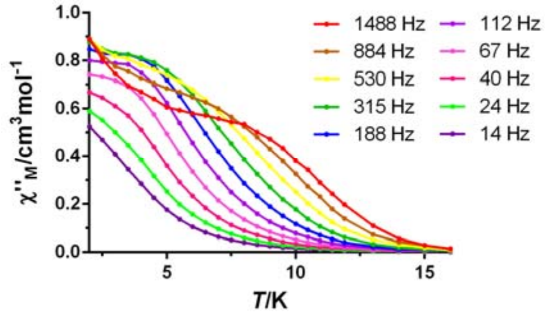

Fig. 7. Temperature dependence of χ''_M for **3** in H_{dc} = 3000 Oe at different frequencies.

The fit of the Cole-Cole plot to a generalised Debye model gives α parameters between 0.39 and 0.16 (Fig. S15, Table S8), which also agree with the presence of more than one relaxation pathways. Thus, Fig. 8 shows that the Arrhenius plot is best fitted with equation 1 once again, yielding values of U_{eff} of 31.0(7) K, with a τ_0 factor of 4.2(3)x10^{-6} s, and τ_{QTM} of 0.51 ms. Alternative fits, including Direct and/or Raman processes, do not allow reproducing the curve properly.

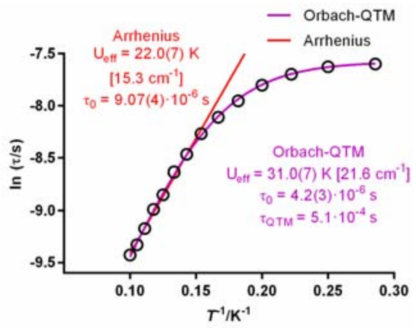

Fig. 8. Arrhenius plot for **3** in a dc applied field of 3000 Oe. The violet line accounts for the best fit considering Orbach plus QTM relaxation (eq. 1).

As it can be seen in Fig. S10, **1**·H_2O does not show χ''_M peaks as a function of the temperature, but frequency dependence of χ''_M in an external field of 2000 G. This phenomenon might be due to the existence of a very small thermal energy barrier to block the magnetisation above 2 K, and/or owing to the occurrence of a rapid QTM relaxation process, which the dc field is not able to eliminate. Therefore, efforts were made to know the origin of the non-SMM like behaviour for **1**·H_2O in the presence of a dc field. As the QTM can be induced by spin-spin interactions, attempts to prepare the diluted yttrium complex $[Dy_{0.09}Y_{0.91}(HL)(NO_3)_2]$ were carried out. However, as it was discussed, these endeavours lead to the isolation of $(Et_3NH)[Dy_{0.09}Y_{0.91}(L)(NO_3)_2]$ (**4**), but the desired compound could not be obtained regardless of the multiple attempts. Besides, the yttrium analogue of **1**·H_2O could not also be isolated, as previously discussed.

Likewise, the dynamic magnetic properties of **4** were studied (Fig. S16 and S17). It should be noted that for **4** χ''_M shows peaks as a function of the temperature and frequency in the absence of an external dc field (Fig. S17). Nevertheless, the tail of this curve does not tend to zero, indicating that the QTM is still efficient at a zero field, in spite of the diluted nature of the sample. This shows the intrinsic QTM of these complexes, which was confirmed by electronic structure calculations (vide infra).

Fitting the Cole−Cole plot to the generalised Debye model gives a series of α parameters below 0.41 (Fig. S18, Table S8), suggesting multiple path relaxation processes. Consequently, many attempts were made to fit the Arrhenius plot but, again, the best fit with coherent parameters was found with equation 1 (Fig. S19), giving values of U_{eff} = 49.1(9) K, τ_0 = 3.6(3)x10^{-8} s, and τ_{QTM} = 0.18 ms.

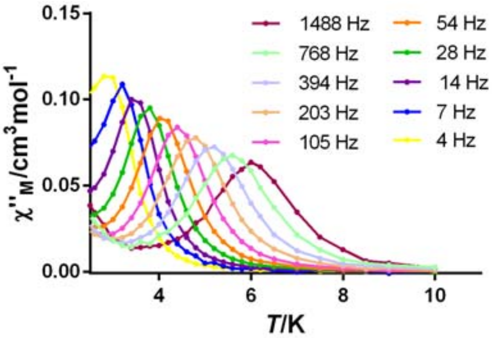

Fig. 9. Temperature dependence of χ''_M for **4** in a dc applied field of 1500 Oe at different frequencies.

The ac magnetic susceptibility data for **4** were additionally measured in the presence of an applied field of 1500 Oe, in order to shortcut the quantum tunnelling (Figs. 9 and S16).

The Arrhenius plot extracted from these data can only be fitted with equation 2 (Fig. 10), which considers Orbach and Raman effects, and that agrees with the presence of more than one relaxation process suggested by the Cole-Cole plot fitting (α = 0.18-0.14, Fig. S18, Table S8).

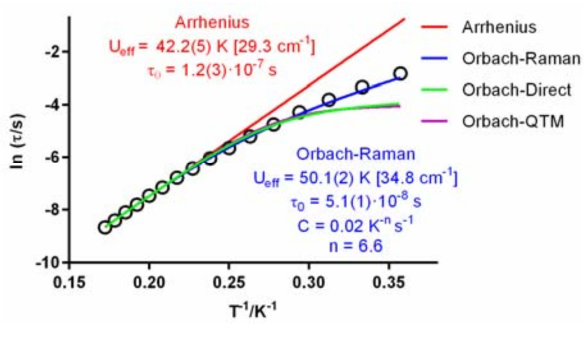

Fig. 10. Arrhenius plot for **4** in a dc applied field of 1500 Oe. The coloured solid lines account for the best fit considering different relaxation processes.

$$\tau^{-1} = CT^{-n} + {\tau_0}^{-1}\mathrm{e}^{-U_{eff}/k_B\mathrm{T}} \quad (2)$$

The best fit yields basically the same U_{eff} value (50.1(2) K) as in the absence of dc field, with an enhanced relaxation time of 5.1(1)x10^{-8} s.

Electronic Structure calculations

CASSCF calculations including spin-orbit effects with the RASSI approach (see Computational details section) were employed in order to explain the magnetic properties of the synthesised compounds. Due to the relatively large ionic character of the dysprosium-ligand bonds, and the large number of unpairedelectrons, dynamic correlation effects are not crucial to describe such systems.[49-51] We have considered six molecular structures: **1** with (**1w**) and without (**1wo**) the whole pyridine molecule, **2**, **3** (the **3a** cation and **3b** anion) and **4** (see Fig. 11). The used methodology, which was widely employed to study this kind of system,[51-53] provides a reasonable agreement with the experimental susceptibility and magnetisation curves (see Figs. S20 and S21). However, some differences are observed at low temperature, especially for compound **2**. In the case of **2**, a water molecule is directly coordinated to the Dy ion, and the uncertainty generated by the H positions might be the responsible of the differences.[54]

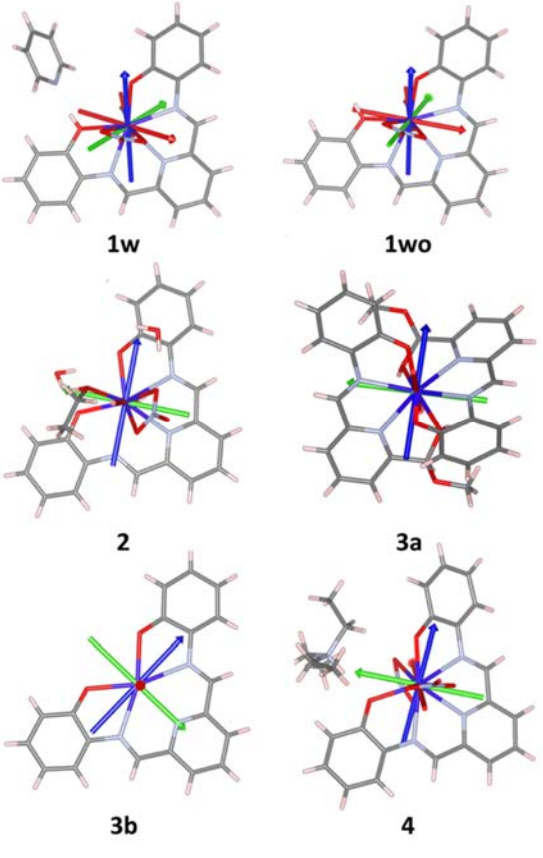

Fig. 11. Representation of the directions of the *g* components for the six calculated systems. The easy axis direction is represented with the blue arrow. Green and red arrows indicate the direction of the g_y and g_x components.

The main calculated parameters for the six systems are collected in Tables 1 and 2. As expected, it can be seen from the calculated *g*-factors that all these Dy^{III} systems present easy-axis character. The direction of the easy axis is determined by the spatial distribution of the ligands. The oblate shape of the electron density expected for Dy^{III} centre ($^6H_{15/2}$ M_J = 15/2 ground state) is an axially-compressed disc that is accommodated in the molecules to reduce the metal-ligand electrostatic repulsion.[50-51] It is worth noting that both **1w** and **1wo** systems are those showing the largest axial character from the calculated *g* values. Furthermore, also the energies are consistent with such conclusion. The excitation energies without spin-orbit contribution indicate the degree of mixing of the excited states with the ground state when the spin-orbit coupling is included.

Table 1. Calculated first and second excitation energies with (E_{SO-1} and E_{SO-2}) and without (E_1 and E_2) spin-orbit effect (cm^{-1}) and $(E_2-E_1)/E_1$ parameter for the six studied systems

Compound	E_1	E_2	$(E_2-E_1)/E_1$	E_{SO-1}	E_{SO-2}
1w	10.4	247.0	22.8	173.2	301.5
1wo	11.1	260.8	22.5	186.3	299.9
2	5.5	100.9	17.3	55.8	195.2
3a	22.0	105.7	3.8	27.5	103.4
3b	7.2	42.0	4.8	107.1	140.9
4	17.3	112.8	5.5	82.2	180.6

Previously, some of us noticed that the figure of merit of the axiality is $(E_2-E_1)/E_1$.[50-51] Large $(E_2-E_1)/E_1$ values results in large anisotropy because the first excited state has a relatively large axial character, like the ground state, but the second excited state is much less axial (see representation of the beta electron densities in Figs. S22 and S23). Thus, first excitation energy for complex **1** is similar to that of the other systems while the second excitation energy is almost twice than in the other systems (see Table 1). And this occurs for both **1w** and **1ow**, which have very similar parameters, thus showing that in this case the presence of different solvates does not affect the magnetic results significantly.

3b is slightly different from the other complexes, due to the presence of two chloride anions with weaker ligand field, and furthermore, the pentadentate ligand is almost perfectly flat while in the other complexes such ligand is slightly distorted (see X-ray discussion).

The magnetic properties are closely related with the adopted structures by these compounds. Thus, if there is a shortest metal-ligand bond distance, the oblate density is perpendicular to such bond to reduce the metal-ligand electron repulsion and consequently, the easy axis is approximately aligned with such bond (see Figs. 11, S22 and S23).

The analysis of the shapes of the beta density of the lowest manifold states at CASSCF level without spin-orbit effect (see Figs. S22 and S23) gives a qualitative picture of the oblate character of the electron density. A weighted mixing of such spin-free states induced by the spin−orbit coupling will result in the ground state of the system that will determine the magnetic properties. In Fig. 11, the orientations of the *g*-components are represented for the six systems. For **1**, the shortest metal-ligand bonds are those through the non-protonated phenolic group. Thus, for both **1w** and **1wo**, the easy-axis is almost perfectly aligned with the shortest Dy-O bond (2.240 Å bond distance) of the unique non-protonated phenolic group (see Fig. 11). However, for the other compounds, there are always two non-protonated phenolic groups with the shortest metal-ligand distances, and the O-Dy-O bond angles are close to 90° (95.2, 95.2 and 102.4° for **2**, **3a** and **4**, respectively). Hence, the oblate disc cannot be easily accommodated within these two oxygen atoms with the shortest Dy-O distances, resulting in a decrease of the axial character of the ground state. The **3b** molecule has easy-axis character placed in the plane of the flat equatorial ligand (see Fig. 11), but not aligned with the chloride donors. Accordingly, these auxiliary chloride ligands do not allow aligning the magnetic axis with the apical geometric axis. Besides, in **3b** the oblate electron density (see Fig. S23) has less metal-ligand repulsion than in the other complexes with more distorted structures. Thus, this system has a larger axiality than the other molecules with two short Dy-O distances.

As a conclusion of these studies, it can be said that the results show that the presence of only one non-protonated phenolic group, as shown in compound **1**, favours axiality because the electron density is easier to accommodate. However, **1**·H_2O does not show a maximum in χ''_M. Therefore, in order to gain more insight into the relaxation paths of these compounds, their qualitative *ab initio* blocking barriers have been computed (Fig. 12).

In compound **1**, the tunnelling probability between the first excited states is large due to the larger value of its transverse components of the g tensor (g_x and g_y), Table 2, which gives to a faster relaxation than in more axial compounds. This might be the reason for the non-observation of a maximum in χ''_M for this compound. In addition, an analysis of collinearity of the easy axis (Table 2) shows that the ground and first excited states are not collinear and that the relaxation can take place through this state. It is worth noting that the combination of the large QTM through the first excited state showed by the electronic structure calculations in combination with the QTM induced by spin-spin interactions might be the responsible of the lack of maximum in the χ''_M curves even in the presence of an applied external dc field.

Table 2. Calculated *g*-factors of the ground and first excited states and the angle between their g_z vectors for the six studied systems.

Compound	g_x	g_y	g_x	γ (°)
1w	19.650	0.030	0.017	
	17.474	0.368	0.319	22.9
1wo	19.662	0.029	0.013	
	17.373	0.378	0.313	20.9
2	18.627	0.079	0.024	
	16.020	0.060	0.004	12.6
3a	14.722	3.839	0.692	
	12.647	4.343	0.479	16.6
3b	19.448	0.068	0.027	
	13.300	2.376	0.927	2.3
4	18.881	0.137	0.052	
	16.349	0.673	0.566	10.6

In the case of **2**, both ground and first excited states have very small transverse components g_x and g_y (Table 2) and the relaxation takes place through the third excited state situated at more than 300 cm^{-1}. Experimentally, an Orbach process was observed, but with a much smaller energy barrier, although this compound has the largest barrier of the studied non-diluted compounds. In comparison with **1**, maxima in χ''_M were observed for **2**, which indicated a larger energy barrier and/or smaller QTM. And the results from the calculations show both tendencies. However, there is a discrepancy between experimental and calculated energy barriers, and an external magnetic field is needed for the observation of SIM-like behaviour in **2**·2H_2O. Both facts might be related to the same reason, the presence of additional relaxation mechanisms, such as QTM in the ground state, induced by dipolar coupling or vibronic coupling, which are not considered in the calculations.

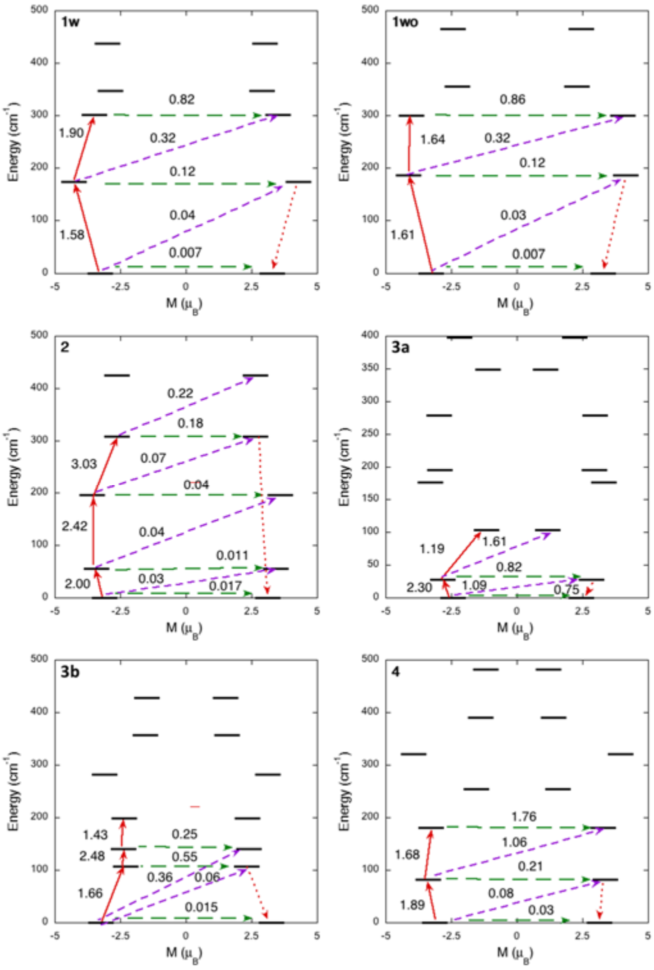

Fig. 12. States energies as a function of their average magnetic moment, M, along the main anisotropy axis for six studied systems. The dashed green arrows correspond to the quantum tunnelling mechanism of ground or excited states, dashed purple arrow shows the hypothetical Orbach relaxation process. The solid red arrow indicates the transition between the ground and excited Kramers doublets and the dashed red arrow the excitation pathway to the ground state with the reversed spin. The values close to the arrows indicate the matrix elements of the transition magnetic moments[29] (above 0.1 an efficient spin relaxation mechanism is expected, see Computational details).

The behaviour of complex **3** is more difficult to rationalise, given that it is formed by two species, **3a** and **3b**. The computational results of both of them individually show an efficient relaxation through the first excited states, which in these cases are relatively close to the ground state. However, the interaction between both complexes can have a very important impact in the relaxation processes, which may explain the different observed experimental behaviour. Besides, compound **4** also shows an efficient relaxation *via* tunneling through the first excited state, with larger transverse components, g_x and g_y.

As a summary, when the data are compared with the experimental results, the same trends are not observed, but this is due to different factors. First of all, the complexity of **3** makes difficult to extract valid correlations from their units **3a** and **3b**. In addition, compound **4** is the only one that is magnetically diluted, thus avoiding dipolar interactions that can suppress the relaxation through tunneling.[55] However, QTM is still observed when no external field is applied, which is due to this efficient tunnelling through the first excited state that is efficiently removed in this case with the application of the external field. In addition, the computational results can explain the observed differences between **1** and **2**, and these calculations lead to conclude that the lack of maximum in χ''_M for **1**, in spite of its axiality, can be due to the more efficient tunneling relaxation. Accordingly, this study shows that axiality is not the only factor to be taken into account in the search for high effective energy barriers.

Conclusions

This work reports the study of the coordination chemistry of dysprosium(III) nitrate and dysprosium(III) chloride with the well-known H_2L ligand, showing that this chemistry is greatly influenced by the operational pH of the medium, and/or by the anion present in metal salt. Thus, mixing of dysprosium(III) nitrate with H_2L allows obtaining two different neutral nitrate complexes, crystallographically characterised, where the Schiff base ligand remains intact. By contrast, the reaction with dysprosium(III) chloride leads to isolate an ionic chloride complex **3**, where the cation shows that the ligand has undergone a partial hydrolysis to form a hemiacetal function, a reaction that has been scarcely reported in literature. These complexes constitute the first lanthanoid compounds derived from H_2L, or related ligands, to be crystallographically characterised, while **3** is also the first hemiacetal complex described with a lanthanoid metal. The crystallographic studies show that the Schiff base acts as a nearly flat pentadentate chelating donor in **1** to **3**, as well as in the dilute complex $(Et_3NH)[Dy_{0.09}Y_{0.91}(L)(NO_3)_2]$ (**4**). Accordingly, this study contributes to the knowledge of the coordination chemistry of lanthanoid complexes with flat polydentate donors. Full magnetic characterisation of **1**·H_2O, **2**·2H_2O, **3** and **4** reveals that only **4** is a SIM at zero dc field, with an U_{eff} about 50 K. **2**·2H_2O and **3** show field-induced slow relaxation of the magnetisation, the largest effective energy barrier of 46.1(9) K being achieved by **2**·2H_2O. However, **1**·H_2O only shows frequency dependence of χ''_M in an external field of 2000 Oe, but not field-induced SIM-like behaviour could be demonstrated. This difference in slow relaxation of the magnetisation is explained in light of *ab initio* calculations, which demonstrate more axiality, but also more efficient relaxation pathways through a tunnelling mechanism for **1** compared with **2**. Accordingly, this study clearly demonstrates that axiality is not the only factor that should be considered for obtaining high performance SIMs, and that alternative approaches to remove the quantum tunnelling should be sought.

Conflicts of interest

There are no conflicts to declare.

Acknowledgements

Authors thank the Spanish Ministerio de Innovación, Ciencia y Universidades (PGC2018-102052-B-C21, PGC2018-093863-B-C21 and MDM-2017-0767) for financial support. J.C.V thanks Xunta de Galicia for his Ph.D. fellowship. E.R. thanks Generalitat de Catalunya for an ICREA Academia award and for the SGR2017-1289 grant, and S.G.C. for a Beatriu de Pinòs grant. The authors acknowledge computer resources, technical expertise and assistance provided by the CSUC.

References

1. J. Long, Y. Guari, R. A.S. Ferreira, L. D. Carlos and J. Larionova, *Coord. Chem. Rev*., 2018, **363**, 57–70.
2. L. Sorace and D. Gatteschi, Electronic Structure and Magnetic Properties of Lanthanide Molecular Complexes. In *Lanthanides and Actinides in Molecular Magnetism*; Layfield, R., Murugesu, M., Eds.;John Wiley & Sons, 2015.
3. N. Ishikawa, M. Sugita, T. Ishikawa, S. Koshihara, and Y. Kaizu, *J. Am. Chem. Soc.*, 2003, **125**, 8694–8695.
4. J. D. Rinehart, and J. R. Long, *Chem. Sci.*, 2011, **2**, 2078–2085.
5. A. K. Bar, P. Kalita, M. K. Singh, G. Rajaraman and V. Chandrasekhar, *Coord. Chem. Rev*., 2018, **367**, 163–216.
6. Z. Zhu, M. Guo, X-L. Li, J. Tang, *Coord. Chem. Rev*., 2019, **378**, 350–364
7. Y-C. Chen, Liu, L. Ungur, J. Liu, Q-W. Li, L-F. Wang, Z-P. Ni, L. F. Chibotaru, X-M. Chen, M-L. Tong, *J. Am. Chem. Soc*., 2016, **138**, 2829-2837.
8. F-S. Guo, B. M. Day, Y-C. Chen, M-L. Tong, A. Mansikkam-ki and R. A. Layfield, *Science*, 2018, **362**, 1400-1403.
9. (a) F-S. Guo, B. M. Day, Y-C. Chen, M-L. Tong, A. Mansikkam-ki, R. A. Layfield, *Angew. Chem. Int. Ed*., 2017, **56**, 11445–11449. (b) C. A. P. Goodwin, F. Ortu, D. Reta, N. F. Chilton and D. P. Mills, *Nature*, 2017, **548**, 439–442.
10. K. R. McClain, C. A. Gould, K. Chakarawet, J. S. Teat, T. J. Groshens, J. R. Long, and B. G. Harvey, *Chem. Sci*., 2018, **9**, 8492-8503.
11. P. Evans, D. Reta, G. F.S. Whitehead, N. F. Chilton and D. P. Mills, *J. Am. Chem. Soc*., 2019, *141*, 19935−19940.
12. (a) J. Liu, Y-C. Chen, J-L. Liu, V. Vieru, L. Ungur, J-H. Jia, L. F. Chibotaru, Y. Lan, W. Wernsdorfer, S. Gao, X-M. Chen, M-L. Tong, *J. Am. Chem. Soc*., 2016, **138**, 5441–5450. (b) Y-C. Chen, J-L. Liu, Y. Lan, Z-Q. Zhong, A. Mansikkam-ki, L. Ungur, Q-W. Li, J-H. Jia, L. F. Chibotaru, J-B. Han, W. Wernsdorfer, X-M. Chen, M-L. Tong, *Chem. Eur. J.*, 2017, **23**, 5708 – 5715. (c) S. Bala, G-Z. Huang, Z-Y. Ruan, S-G. Wu, Y. Liu, L. F. Wang, J-L. Liu, and M-L. Tong, *Chem. Commun*., 2019, **55**, 9939—9942. (d) A. B. Canaj, S. Dey, E. R. Mart, C. Wilson, G. Rajaraman, M. Murrie, *Angew. Chem*., 2019, **131**, 14284-14289.
13. A. González, E. Gómez, A. Cortés-Lozada, S. Hernández, T. Ramírez-Apan and A. Nieto-Camacho, *Chem. Pharm. Bull.* 2009, *57*, 5—15.
14. D. C. Liles, M. McPartlin, P. A. Tasker, H. C. Lip and L. F. Lindoy, *J. Chem. Soc., Chem. Commun*., 1976, 549-551.
15. K. Potgieter, P. Mayer, T. I. A. Gerber and I. N. Booysen, *Polyhedron* 2009, **28**, 2808–2812.
16. G. Habarurema, T. I. A. Gerber, E. C. Hosten and R. *Z.* Betz, *Kristallogr. NCS*, 2015, 230, 159-161.
17. M. Kose, P. L. Goring, and V. Mckee, *Inorg. Chim. Acta*, 2015, **435**, 232–238.
18. F. F. B. J. Janssen, L. C. J. M. Peters, P. P. J. Schlebos, J. M. M. Smits, R. de Gelder and A. E. Rowan, *Inorg. Chem*. 2013, **52**, 13004−13013.
19. X-X. Sun, C-M. Qi, S-L. Ma, H-B. Huang, W-X. Zhu and Y-C. Liu, *Inorg. Chem. Commun*., 2006, **9**, 911–914.
20. M. Kose, *Inorg. and Nano-Metal Chem*., 2017, **47**, 1711-1717.
21. E. Kampert, F. F. B. J. Janssen, D. W. Boukhvalov, J. C. Russcher, J. M. M. Smits, R. de Gelder, B. de Bruin, P. C. M. Christianen, U. Zeitler, M. I. Katsnelson, J. C. Maan and A. E. Rowan, A. E. *Inorg. Chem.*, 2009, **48**, 11903–11908.
22. *SADABS: Area-Detector Absorption Correction*. Siemens Industrial Automation, Inc.: Madison, WI, 1996.
23. G. M. Sheldrick, *Acta Crystallogr., Sect. A: Found. Crystallogr*., 2008, **A64**, 112−122.
24. P-Å. Malmqvist, B. O. Roos and B. Schimmelpfennig, *Chem. Phys. Lett*., 2002, **357**, 230-240.
25. B. O. Roos, R. Lindh, P-Å. Malmqvist, V. Veryazov, P-O- Widmark and A. C. Borin, *J. Phys. Chem*. A, 2008, **112**, 11431-11435.
26. B. O. Roos, R. Lindh, P-Å. Malmqvist, V. Veryazov and P-O. Widmark, *J. Phys. Chem. A*, 2004, **108**, 2851-2858.
27. P-O. Widmark, P-Å. Malmqvist, B. O. Roos, *Theor. Chim. Acta*, 1990, **77**, 291-306.
28. I. Fdez. Galván, M. Vacher, A. Alavi, C. Angeli, F. Aquilante, J. Autschbach, J. J. Bao, S. I. Bokarev, N. A. Bogdanov, R. K. Carlson, L. F. Chibotaru, J. Creutzberg, N. Dattani, M. G. Delcey, S. S. Dong, A. Dreuw, L. Freitag, L. M. Frutos, L. Gagliardi, F. Gendron, A. Giussani, L. González, G. Grell, M. Guo, C. E. Hoyer, M. Johansson, S. Keller, S. Knecht, G. Kovačević, E. Källman, G. Li Manni, M. Lundberg, Y. Ma, S. Mai, J. P. Malhado, P. A. Malmqvist, P. Marquetand, S. A. Mewes, J. Norell, M. Olivucci, M. Oppel, Q. M. Phung, K. Pierloot, F. Plasser, M. Reiher, A. M. Sand, I. Schapiro, P. Sharma, C. J. Stein, L. K. Sørensen, D. G. Truhlar, M. Ugandi, L. Ungur, A. Valentini, S. Vancoillie, V. Veryazov, O. Weser, T. A. Wesołowski, P-O. Widmark, S. Wouters, A. Zech, J. P. Zobel, R. Lindh, R. *J. Chem. Theor. Comput.*, 2019, **15**, 5925-5964.
29. L. Ungur and L. Chibotaru, *Inorg. Chem.*, 2016, **556**, 10043-10056.
30. D. Drahonovsky and J-M. Lehn, *J. Org. Chem*., **2009**, *74*, 8428–8432.
31. A. M. Guidote Jr. K. Ando, Y. Kurusu, H. Nagao and Y. Masuyama, *Inorg. Chim. Acta*, 2001, **314**, 27–36.
32. A. Erxleben, *Inorg. Chim. Acta*, 2009, **362**, 839–844.
33. J. G. Małecki and P. Zwolinski, *Polyhedron*, 2012, **39**, 85–90.
34. A. Barandov, and U. Abram, *Z. Anorg. Allg. Chem*., 2013, **639**, 2542–2547.
35. A. A. Melekhova, A. S. Novikov, N. V. Rostovskii, P. A. Sakharov, T. L. Panikorovskii and N. A. Bokach, *Inorg. Chem. Commun*., 2017, ***79***, 82-85.

36. D Mondal and K. Bhattacharya, *Inorg. Chem. Commun*., 2017, **84**, 109-112.
37. K. Nakamoto, *Infrared and Raman Spectra of Inorganic and Coordination Compounds*, Ed. John Wiley & Sons, New York, 1997.
38. (a) M. Llunell, D. Casanova, J. Cirera, J. M. Bofill, P. Alemany, S. Alvarez, M. Pinsky and D. D. Avnir, SHAPE v1.1b, Barcelona, 2005; (b) A. Ruiz-Martínez, D. Casanova, S. Alvarez, *Chem. Eur. J*., 2008, **14**, 1291–1303; (c) M. Llunell, D. Casanova, J. Cirera, P. Alemany amd S. Alvarez, SHAPE: Program for the stereochemical analysis of molecular fragments by means of continuous shape measures and associated tools; University of Barcelona, Barcelona, Spain, 2010.
39. M. Fondo, J. Corredoira-Vázquez, A. M. García-Deibe, J Sanmartín-Matalobos, J. M. Herrera and E. Colacio, *Inorg. Chem.*, 2018, **57**, 10100–10110.
40. A. K. Bar, P. Kalita, J-P. Sutter and V. Chandrasekhar, *Inorg. Chem.*, 2018, **57**, 2398−2401.
41. F. H. Allen, The Cambridge Structural Database: a quarter of a million crystal structures and rising. *Acta Crystallogr.*, 2002, **B58**, 380-388.
42. S-Y. Lin, W. Wernsdorfer, L. Ungur, A. K. Powell, Y-N. Guo, J. Tang, L. Zhao, L. F. Chibotaru, H-J. Zhang, *Angew. Chem. Int. Ed.*, 2012, **51**, 12767–12771.
43. (a) M. Fondo, J. Corredoira-Vázquez, A. M. García-Deibe, J Sanmartín-Matalobos, J. M. Herrera and E. Colacio, *Inorg. Chem*., 2017, **56**, 5646-5656. (b) M. Fondo, J. Corredoira-Vázquez, A. Herrera-Lanzós, A. M. García-Deibe, J Sanmartín-Matalobos, J. M. Herrera, E. Colacio and C. Nuñez, *Dalton Trans*., 2017, **46**, 17000–17009.
44. C. Das, A. Upadhyay and M. Shanmugam, *Inorg. Chem*., 2018, **57**, 9002−9011.
45. S. Yu, Z. Hu, Z. Chen, B. Li, Y-Q. Zhang, Y. Liang, D. Liu, D. Yao and F. Liang, *Inorg. Chem*., 2019, **58**, 1191−1200.
46. (a) J. R. Friedman, M. P. Sarachick, J. Tejada, J. and R. Ziolo, *Phys. Rev. Lett*., 1996, **76**, 3830–3833; (b) L. Thomas, F. Lionti, R. Ballou, D. Gatteschi, R. Sessoli and B. Barbara, *Nature*, 1996, **383**, 145–147.
47. J. Ruiz, A. J. Mota, A. Rodríguez-Diéguez, S. Titos, J. M. Herrera, E. Ruiz, E. Cremades, J. P. Costes and E. Colacio, *Chem. Commun*., 2012, **48**, 7916-7918.
48. B. M. Day, F-S. Guo and R. A. Layfield, *Acc. Chem. Res*., 2018, **51**, 1880−1889, and references therein.
49. N. F. Chilton, D. Collison, E. J. L. McInnes, R. E. P. Winpenny and A. Soncini, *Nat. Commun.*, 2013, **4**, 2551.
50. D. Aravena and E. Ruiz, *Inorg. Chem.*, 2013, **52**, 13770-13778.
51. S. Gomez-Coca, D. Aravena, R. Morales, E. Ruiz, *Coord. Chem. Rev.*, 2015, **289**, 379-392.
52. M. Atanasov, D. Aravena, E. Suturina, E. Bill, D. Maganas and F. Neese, *Coord. Chem. Rev.*, 2015, **289**, 177-214.
53. J. P. Malrieu, R. Caballol, C. J. Calzado, C. de Graaf, N. Guihéry, *Chem. Rev.*, 2014, **114**, 429-492.
54. G. Cucinotta, M. Perfetti, J. Luzon, M. Etienne, P-E. Car, A. Caneschi, G. Calvez, K. Bernot, R. Sessoli, *Angew. Chem.*, 2012, **124**, 1638-1642.
55. D. Aravena, *J. Phys. Chem. Lett.*, 2018, **9**, 5327-5333.